

LETTER TO THE EDITOR

First results of the *Herschel* Key Program ‘Dust, Ice and Gas in Time’: Dust and Gas Spectroscopy of HD 100546*

B. Sturm¹, J. Bouwman¹, Th. Henning¹, N. J. Evans II², B. Acke^{10, **}, G. D. Mulders^{3, 20}, L. B. F. M. Waters^{3, 10}, E. F. van Dishoeck^{4, 6}, G. Meeus⁵, J. D. Green², J. C. Augereau⁹, J. Olofsson¹, C. Salyk², J. Najita¹⁴, G. J. Herczeg⁶, T. A. van Kempen⁷, L. E. Kristensen⁴, C. Dominik^{3, 21}, J. S. Carr¹³, C. Waelkens¹⁰, E. Bergin¹⁷, G. A. Blake¹², J. M. Brown⁶, J.-H. Chen², L. Cieza^{16, ***}, M. M. Dunham², A. Glassgold¹⁸, M. Güdel¹⁹, P. M. Harvey², M. R. Hogerheijde⁴, D. Jaffe², J. K. Jørgensen²², H. J. Kim², C. Knez¹⁵, J. H. Lacy², J.-E. Lee¹¹, S. Maret⁹, R. Meijerink⁴, B. Merín⁸, L. Mundy¹⁵, K. M. Pontoppidan¹², R. Visser⁴, and U. A. Yildız⁴

(Affiliations can be found after the references)

Preprint online version: June 24, 2021

ABSTRACT

Context. We present far-infrared spectroscopic observations, taken with the Photodetector Array Camera and Spectrometer (PACS) on the *Herschel* Space Observatory, of the protoplanetary disk around the pre-main-sequence star HD 100546. These observations are the first within the DIGIT *Herschel* key program, which aims to follow the evolution of dust, ice, and gas from young stellar objects still embedded in their parental molecular cloud core, through the final pre-main-sequence phases when the circumstellar disks are dissipated.

Aims. Our aim is to improve the constraints on temperature and chemical composition of the crystalline olivines in the disk of HD 100546 and to give an inventory of the gas lines present in its far-infrared spectrum.

Methods. The 69 μm feature is analyzed in terms of position and shape to derive the dust temperature and composition. Furthermore, we detected 32 emission lines from five gaseous species and measured their line fluxes.

Results. The 69 μm emission comes either from dust grains with ~ 70 K at radii larger than 50 AU, as suggested by blackbody fitting, or it arises from ~ 200 K dust at ~ 13 AU, close to the midplane, as supported by radiative transfer models. We also conclude that the forsterite crystals have few defects and contain at most a few percent iron by mass. Forbidden line emission from [C II] at 157 μm and [O I] at 63 and 145 μm , most likely due to photodissociation by stellar photons, is detected. Furthermore, five H₂O and several OH lines are detected. We also found high- J rotational transition lines of CO, with rotational temperatures of ~ 300 K for the transitions up to $J = 22 - 21$ and $T \sim 800$ K for higher transitions.

Key words. star: HD 100546 – infrared – young stellar objects – spectroscopy

1. Introduction

Circumstellar disks around young stars are the birthplaces of planetary systems. To understand planet formation, it is vital to study the processes that govern the evolution of gas and dust in these disks. PACS provides unique information in this field through observations of far-infrared (IR) solid-state features which are particularly sensitive to temperature and elemental composition. Moreover, PACS is well suited to study the warm gas of a few 100 K, complementary to the hot gas probed in near-IR and the cold gas observed at millimeter wavelengths.

An intensively studied pre-main-sequence star is the Herbig B9.5Vne star HD 100546. While signs of ongoing accretion indicate the star’s infancy (Deleuil et al. 2004), the estimated age of 10 Myr makes it unusually old for a star with a disk (van den Ancker et al. 1997). HD 100546 is nearby (103 pc) and optical/near-IR scattered light imaging has revealed a wealth of structures in the disk (e.g., Grady et al. 2001; Augereau et al. 2001; Ardila et al. 2007). Based on the mid- to near-IR excess

ratio, Bouwman et al. (2003) suggested an inner cavity in the disk. Later observations confirmed this gap (e.g., Grady et al. 2005; Benisty et al. 2010). This remarkable feature and the longevity of the HD 100546 disk may point to a young planet in the inner 10 AU, making it a prime target for detailed studies.

The system of HD 100546 has a rich 2.4 – 180 μm spectrum as observed with ISO (Malfait et al. 1998), showing a striking similarity with that of the comet Hale-Bopp (Crovisier et al. 1997). Juhász et al. (2010) investigated the *Spitzer* spectrum of the source. Strong forsterite emission is observed in both ISO and *Spitzer* data. A continuum fit indicated crystalline dust at 210 K and 50 K (Malfait et al. 1998).

The ISO spectrum shows a strong line of [O I] 63 μm and a weaker [C II] 158 μm line. In the near-IR, Brittain et al. (2009) and van der Plas et al. (2009) observed CO ro-vibrational lines with a rotational temperature of ~ 1000 K and found no CO gas in the inner dust cavity. Observations of optical [O I] and Balmer line emission, on the other hand, demonstrate that the inner disk is not completely devoid of gas (Acke & van den Ancker 2006). At submillimetre wavelengths, Panić et al. (2010) have detected pure rotational lines of CO up to $J = 7 - 6$ probing a warm (60–70 K) layer in the outer disk (~ 100 AU). Information on the intermediate temperatures is still lacking.

Here we present an analysis of narrow features (about 1 μm) in the far-IR spectrum of HD 100546 over the full PACS range

Send offprint requests to: B. Sturm, e-mail: sturm@mpia.de

* *Herschel* is an ESA space observatory with science instruments provided by European-led Principal Investigator consortia and with important participation from NASA.

** Postdoctoral Fellow of the Fund for Scientific Research, Flanders

*** *Spitzer* Fellow

that was obtained within the *Herschel* key program ‘Dust, Ice and Gas in Time’ (DIGIT).

2. Observation and data reduction

We used the spectral energy distribution (SED) mode, covering the wavelength range from 55 to 210 μm (see Poglitsch 2010, for details of the instrument and calibration). Four up/down scans of the grating for two nod positions were performed with a chopper throw of 1'. Our data were processed in HIPE 3.0, provided by the *Herschel* science center, up to level 1. We did not apply the integration ramp linearity, cross-talk and response drift corrections as these were not yet scientifically validated.

After level 1 processing, we extracted the spectra for the two nod positions separately from the central spaxel (spatial element). The wavelength-dependent point spread function (PSF) correction was taken from the PACS calibration document PACC-KL-TN-04¹. We first uniformly rebinned the spectra, using an over-sampling factor of 1 relative to the spectral resolution of the instrument and an up-sampling factor of 2, before combining the spectra of the two nod positions. The current flux calibration and relative spectral response function (RSRF) were derived from ground-based measurements. The correction factors, determined from the first in-space calibrations were applied (for details see the PACS calibration document PACC-KL-TN-04¹). We estimate that the absolute flux calibration is accurate within 30%. The RSRF is valid for spectral features not much wider than about 1 μm . For broader features, the RSRF is not yet well calibrated. Therefore, we will focus on spectral features narrower than about 1 μm . The wavelength calibration is accurate down to the spectral resolution as can be seen from the gas-phase lines, most of which are found within 0.02 μm of their laboratory wavelength.

3. Results and Discussion

The PACS data confirm the tentative ISO detection of the 69 μm forsterite band first reported by Malfait et al. (1998) and deliver a band profile of very high quality (see Fig. 1). The feature is characterized by a signal-to-noise ratio of about 10. In addition, we find a wealth of narrow molecular gas lines in the spectrum of HD 100546, coming from CO, H₂O, and OH, and [C II] and [O I] fine-structure lines (see Table 1).

In this section we present an analysis of the 69 μm forsterite peak in terms of dust temperature and composition. In addition, we provide a compilation of the detected gas lines in the far-IR spectrum of HD 100546 and derive the CO-rotational temperature. A full spectral decomposition, including a search for shallow and wide features (e.g. ice and hydrated silicate features), will be presented in a follow-up paper.

3.1. Forsterite

The ‘69 μm ’ band is a characteristic signature of forsterite - the Mg-rich end member of olivines (Henning 2010). In order to determine the position and width of this feature, we fitted a Lorentz profile and a linear function for the continuum (compare e.g., Koike et al. 2006) in the wavelength interval 68–71 μm . The emission peaks at $69.198 \pm 0.008 \mu\text{m}$ and has a FWHM of $0.64 \pm 0.03 \mu\text{m}$.

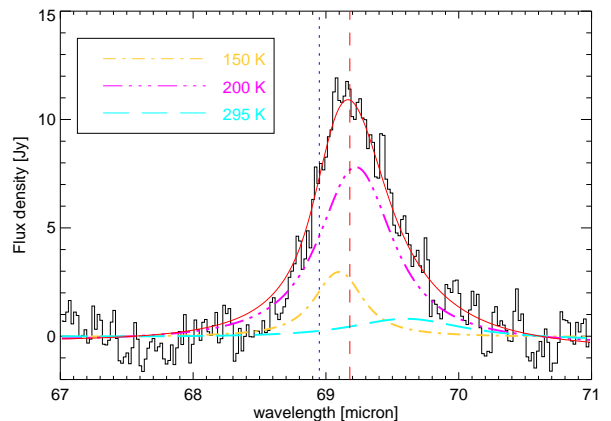


Fig. 1. The continuum-subtracted forsterite emission at 69 μm (histogram) overplotted with the best-fit model (red line) which is given by eq. (1). The contributions of the different temperatures are indicated. The dotted vertical line locates the peak position of 70 K pure forsterite and the dashed one the position in the PACS spectrum, fitted with a Lorentz profile, which is not shown here.

The 69 μm band profile depends on both the temperature and the iron content (e.g., Koike et al. 2006, 2003) of the olivine crystals. Increasing the dust temperature leads to a shift of the peak position towards longer wavelengths and to an increase of the FWHM (Fig. 2). Increasing the iron content in the olivine crystals has a very pronounced effect in shifting the band to longer wavelengths (Fig. 3). Finally, the FWHM will increase with the number of lattice distortions (Koike et al. 2010).

Based on the peak position of the band, we can immediately conclude that the olivines cannot contain more than 3–4% iron as this would cause the peak to appear at significantly longer wavelengths than observed. The PACS observations provide much better constraints on the iron content than the shorter-wavelength *Spitzer* data (Juhász et al. 2010) because silicate bands in that spectral range are less sensitive to a change in Mg/Fe ratio. Furthermore, the small FWHM of the band profile indicates crystals with few defects (Koike et al. 2010). The small FWHM also shows that the dust emission comes from a narrow range of temperatures.

Determining the temperature of the dust that produces the 69 μm feature from intrinsic properties of this band is more difficult because even a small amount of iron could balance a lower temperature. Assuming pure forsterite results in a dust temperature of about 200 K (Fig. 2). To constrain the amount of colder dust, we fitted the observed profile with a weighted sum of laboratory data (Suto et al. 2006) at different temperatures, ranging from 50–300 K (Fig. 1). The measured flux $F_{68-71\mu\text{m}}$ is given by

$$F_{68-71\mu\text{m}}(\lambda) = F_{\text{cont}}(\lambda) + \sum_{i=1}^5 w_i \cdot \kappa(T_{\text{dust}}^i, \lambda) \cdot B_{\lambda}(\lambda, T_{\text{dust}}^i). \quad (1)$$

Here F_{cont} is the local continuum, and the κ values are the mass absorption coefficients, computed from the optical constants of the Suto et al. (2006) forsterite sample, at the different dust temperatures T_{dust}^i . Finally, the w_i values are the relative weights of the flux at the different temperatures. In addition, we had to specify a dust shape distribution in order to calculate the mass absorption values. We used the DHS model (distribution of hollow spheres, Min et al. 2003) with a grain size of 0.1 μm , which has been found to be a good representation of observed silicate profiles (e.g., Juhász et al. 2010).

¹ http://herschel.esac.esa.int/Docs/Calibration/PACS_SpectroscopyPerformanceCalibration_11Mar2010.pdf

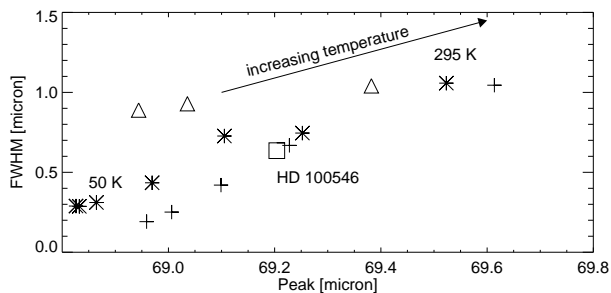


Fig. 2. FWHM of the forsterite ‘69 μm band’ plotted over the peak position, fitted with a Lorentz profile. The square is our HD 100546 data (size indicates error). For comparison, data from Koike et al. (2006, asterisks: ‘Kyoto sample’, triangles: ‘Jena sample’), Suto et al. (2006, crosses, DHS with 0.1 μm grainsize) are shown.

Under the assumption of pure forsterite, no more than a few percent of the dust emission can be coming from the 50 K component. This could be up to 9%, if grains of $\sim 5 \mu\text{m}$ radius are assumed. Such large grains can only exist in the deeper layers of the disk, where they are invisible to *Spitzer*, as Juhász et al. (2010) rule out grains $\geq 1 \mu\text{m}$. The bulk of the emission, under the assumption of pure forsterite, comes from $\sim 150\text{--}200 \text{ K}$.

However, a temperature of 150 to 200 K for the 69 μm band would lead to tremendously higher fluxes in the 20–40 μm region than observed by ISO and *Spitzer*. Additionally, the predicted relative strength between the 24– and 33 μm forsterite bands would be inverted compared to the observations. In fact, temperatures of only 70 K (Bouwman et al. 2003) or even 50 K (Malfait et al. 1998) were derived from the ISO data.

These results can be reconciled in two ways. First, the dust producing the 69 μm feature is at 70–50 K. The shift from the band position in the 70–50 K laboratory data to the one observed by PACS could be caused by an admixture of iron. Given the information in Fig. 3, we need at least 2 but no more than 3% for such a shift, considering that the data were taken at $\sim 300 \text{ K}$.

An alternative explanation is based on the optical depth of the disk which decreases with increasing wavelength. The $\tau = 1$ surface is deep into the disk at 69 μm , even reaching the midplane (Mulders 2010). The disk of HD 100546 is a special case in this respect: because of its large inner hole, the midplane temperature at 13 AU is much higher ($\sim 150\text{--}200 \text{ K}$) than in disks without a hole so that the far-infrared features can be produced in heated layers close to the midplane from which the radiation at 70 μm can escape. In the most extreme case the emission could arise from pure forsterite of 200 K temperature, located in the midplane at 13 AU.

In this scenario the location of the forsterite near the inner edge of the disk supports the crystallization by collisional cascades or shocks induced by the suggested giant planet.

3.2. Gas lines

We identified 32 gas lines (Table 1) from the ISO line lists². CO lines up to the $J=31\text{--}30$ transition were detected as well as H₂O and OH lines. Selected molecular lines are shown in Fig. 4. Furthermore, we confirm the ISO detections of [O I] and [C II] fine-structure lines (Lorenzetti et al. 2002). The integrated line fluxes, obtained from fitted Lorentz profiles, are in Table 1. The [O I] line fluxes agree within 30% with those seen by

² <http://www.mpe.mpg.de/ISO/linelists/index.html>

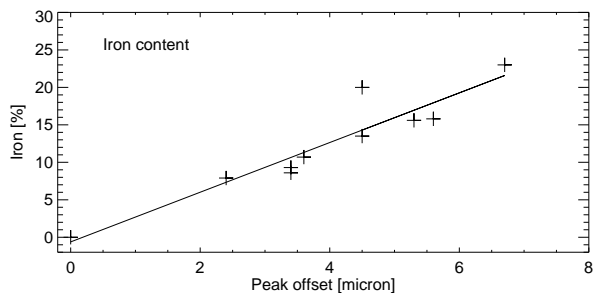


Fig. 3. Effect of iron-rich olivines on the peak wavelength of the ‘69 μm ’ band at room temperature. The offset in wavelength is relative to pure forsterite. The data are from Koike et al. (2003) and the line is the best-fit linear function.

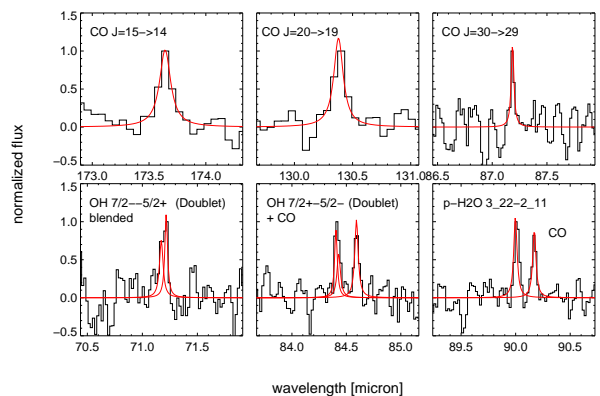


Fig. 4. Selected gas lines from the PACS spectrum of HD 100546. The continuum-subtracted, normalized fluxes are plotted as histograms. The continuum has been fitted with a linear function of the wavelength and the peaks with Lorentz profiles. The second peak in the H₂O 90 μm panel is CO $J=29\text{--}28$.

ISO (Lorenzetti et al. 2002), while the [C II] line flux is about a factor of 3 weaker. Significant flux outside the pointsource PSF is detected for the [C II] line, which is not seen for any other line, suggesting that extended emission dominates the larger ISO beam. Through comparison of the flux ratios $[\text{O I}]_{63}/[\text{O I}]_{145}$ and $[\text{O I}]_{63}/[\text{C II}]_{158}$ with the models from Kamp et al. (2010) a gas mass of $\sim 10^{-3} M_{\odot}$ is derived.

According to our knowledge, the detection of H₂O is one of the first in the disk of a Herbig Ae/Be star. The emission seems to emerge from optically thick gas. A possible source for the H₂O could be sublimation of water ice. A detailed analysis will be presented in a future paper.

Our focus here is on the newly detected CO lines. In Fig. 5 we show the rotational diagram of the CO lines. Although a single-temperature $T = 580 \pm 14 \text{ K}$ provides a reasonable fit (reduced $\chi^2 = 15$) to the data, a better representation could be obtained by a two-temperature model (reduced $\chi^2 = 1.8$). The transitions up to $J=22\text{--}21$ are fitted by $T = 300 \pm 12 \text{ K}$. The higher rotational transitions require a hotter gas component of $800 \pm 100 \text{ K}$ providing the connection to the high-temperature gas in the innermost part of the disk detected by near-infrared spectroscopy (Brittain et al. 2009; van der Plas et al. 2009). This inferred temperature range is consistent with CO in a heated surface layer of the disk as found in disk models that do not assume equal gas and dust temperatures but include an explicit treatment

Species	Transition	Peak [μm]	Lineflux $10^{-17}[\text{W}/\text{m}^2]$
[O I]	$^3\text{P}_1 - ^3\text{P}_2$	63.19	554.37 ± 5.0
[O I]	$^3\text{P}_0 - ^3\text{P}_1$	145.54	35.70 ± 1.3
[C II]	$^2\text{P}_{3/2} - ^2\text{P}_{1/2}$	157.75	31.87 ± 1.0
CO	$J = 14 - 13$	186.01	7.42 ± 0.9
CO	$J = 15 - 14$	173.64	11.50 ± 0.8
CO	$J = 16 - 15$	162.82	8.25 ± 0.9
CO	$J = 17 - 16$	153.28	10.49 ± 0.8
CO	$J = 18 - 17$	144.79	9.85 ± 1.0
CO	$J = 19 - 18$	137.21	8.86 ± 0.7
CO	$J = 20 - 19$	130.38	7.10 ± 0.7
CO	$J = 21 - 20$	124.18	5.94 ± 0.6
CO	$J = 22 - 21$	118.59	5.92 ± 0.9
CO ¹	$J = 23 - 22$	113.47	4.76 ± 1.2
CO	$J = 24 - 23$	108.77	10.56 ± 1.3
CO	$J = 26 - 25$	100.47	12.71 ± 2.4
CO	$J = 27 - 26$	96.78	10.20 ± 1.4
CO	$J = 28 - 27$	93.35	10.00 ± 1.0
CO	$J = 29 - 28$	90.17	11.83 ± 1.6
CO	$J = 30 - 29$	87.19	8.46 ± 1.0
CO ¹	$J = 31 - 30$	84.40	4.90 ± 1.5
OH	$3/2, 9/2^+ - 7/2^-$	65.29	10.00 ± 1.5
OH ¹	$1/2, 7/2^- - 5/2^+$	71.17	9.17 ± 1.4
OH ¹	$1/2, 7/2^+ - 5/2^-$	71.22	10.10 ± 1.1
OH ¹	$3/2, 7/2^+ - 5/2^-$	84.42	14.96 ± 1.7
OH	$3/2, 7/2^- - 5/2^+$	84.59	14.96 ± 1.5
OH	$1/2, 5/2^+ - 3/2^-$	98.73	8.74 ± 1.5
OH	$1/2, 3/2^- - 1/2^+$	163.41	2.60 ± 0.6
p-H ₂ O	$3_{22} - 2_{11}$	90.00	14.32 ± 1.2
o-H ₂ O ¹	$4_{14} - 3_{03}$	113.53	3.64 ± 0.9
o-H ₂ O	$3_{30} - 3_{21}$	136.48	4.52 ± 0.7
p-H ₂ O	$3_{13} - 2_{02}$	138.54	3.17 ± 0.7
o-H ₂ O	$2_{12} - 1_{01}$	179.54	5.53 ± 0.8

¹ deblended lines, CO not used in rotational diagram

Table 1. Peak wavelengths and line fluxes for the identified gas lines between 60 and 190 μm . Only the formal errors are given, not including systematic errors due to the PACS spectral response function.

of the heating and cooling processes (e.g., Kamp & Dullemond 2004). The 300 K component could also emerge from the region in the midplane close to the gap.

According to Brittain et al. (2009) the 4.7 μm CO fundamental emission shows both a UV fluorescent and a thermal component. The latter was fitted with a column density of at least $2.3 \cdot 10^{15} \text{ cm}^{-2}$ (for discussion, see Brittain et al. 2009). The submillimeter data give a typical CO column density of 10^{18} cm^{-2} (Panić et al. 2010). From Fig. 5, assuming that the emission originates from the area between 13 and 100 AU, we derive column densities of 10^{16} to 10^{17} cm^{-2} in both models. These values indicate that PACS probes the part of the disk between the near-IR and submillimeter data.

4. Conclusions

The PACS data provide the strongest constraints yet on the composition of olivines in a protoplanetary disk. We found the olivines to be extremely iron-poor (less than 3–4% iron). Our observations can be modeled with dust at ~ 70 K, consistent with ISO results, but requiring at least 2% iron. On the other hand the determination of the temperature of the forsterite based on intrinsic features of the 69 μm band instead of using a continuum analysis offers a second option: The emission may emerge from

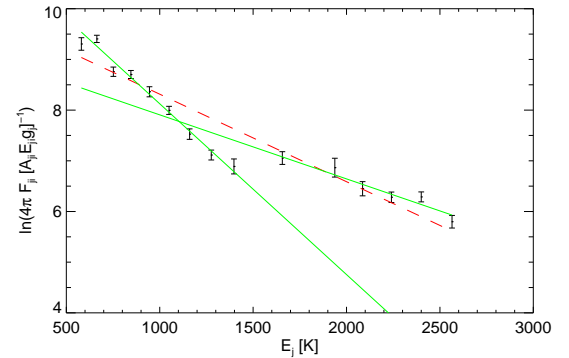


Fig. 5. Rotational diagram of the CO lines in HD 100546 (crosses), overplotted with our models, using eq. 2 from Justtanont et al. (2000). A single temperature fit (dashed) gives reasonable results, but a two-temperature approach (solid) yields a better description of the data. CO $J=23-22$ and $J=31-30$ are blended with H₂O and OH respectively and were not used in the fit, nor are they shown here.

pure forsterite at 200 K and 13 AU close to the midplane. This region is optically thick for shorter wavelengths.

The far-infrared spectrum of HD 100546 contains a wealth of molecular gas lines including CO, H₂O, and OH. We found CO transitions up to $J=31-30$ which arise from gas in the temperature range of 300 to 800 K and appear to sample gas in the surface layers of the disk at temperatures and surface densities intermediate to those probed by submillimeter and near-infrared CO measurements.

Acknowledgements. Support for this work, part of the *Herschel* Open Time key program, was provided by NASA through an award issued by the Jet Propulsion Laboratory, California Institute of Technology. G. Meeus is partly supported by Spanish grant AYA 2008-01727. The authors thank the referee C. Grady for helpful comments that improved the paper.

References

- Acke, B. & van den Ancker, M. E. 2006, *A&A*, 449, 267
Ardila, D. R., Golimowski, D. A., Krist, J. E., et al. 2007, *ApJ*, 665, 512
Augereau, J. C., Lagrange, A. M., Mouillet, D., & Ménard, F. 2001, *A&A*, 365, 78
Benisty, M., Tatulli, E., Ménard, F., & Swain, M. R. 2010, *A&A*, 511, A75+
Bouwman, J., de Koter, A., Dominik, C., & Waters, L. B. F. M. 2003, *A&A*, 401, 577
Brittain, S. D., Najita, J. R., & Carr, J. S. 2009, *ApJ*, 702, 85
Crovissier, J., Leech, K., Bockelee-Morvan, D., et al. 1997, *Science*, 275, 1904
Deleuil, M., Lecavelier des Etangs, A., Bouret, J., et al. 2004, *A&A*, 418, 577
Grady, C. A., Polomski, E. F., Henning, Th., et al. 2001, *AJ*, 122, 3396
Grady, C. A., Woodgate, B., Heap, S. R., et al. 2005, *ApJ*, 620, 470
Henning, Th. 2010, *ARAA*, in press
Juhász, A., Bouwman, J., Henning, Th., et al. 2010, *ApJ*, submitted
Justtanont, K., Barlow, M. J., Tielens, A. G. G. M., et al. 2000, *A&A*, 360, 1117
Kamp, I. & Dullemond, C. P. 2004, *ApJ*, 615, 991
Kamp, I., Tilling, I., Woitke, P., Thi, W., & Hogerheijde, M. 2010, *A&A*, 510, A18+
Koike, C., Chihara, H., Tsuchiyama, A., et al. 2003, *A&A*, 399, 1101
Koike, C., Imai, Y., Chihara, H., et al. 2010, *ApJ*, 709, 983
Koike, C., Mutschke, H., Suto, H., et al. 2006, *A&A*, 449, 583
Lorenzetti, D., Giannini, T., Nisini, B., et al. 2002, *A&A*, 395, 637
Malfait, K., Waelkens, C., Waters, L. B. F. M., et al. 1998, *A&A*, 332, L25
Min, M., Hovenier, J. W., & de Koter, A. 2003, *A&A*, 404, 35
Mulders, G. e. 2010, *ApJ*, in prep.
Panić, O., van Dishoeck, E., Hogerheijde, M., et al. 2010, *A&A*, in press
Poglitsch, A. ??, . 2010, *A&A*, this issue
Suto, H., Sogawa, H., Tachibana, S., et al. 2006, *MNRAS*, 370, 1599
van den Ancker, M. E., The, P. S., Tjin A Djie, H. R. E., et al. 1997, *A&A*, 324, L33
van der Plas, G., van den Ancker, M. E., Acke, B., et al. 2009, *A&A*, 500, 1137

¹ Max Planck Institute for Astronomy, Königstuhl 17, D-69117 Heidelberg, Germany

² The University of Texas at Austin, Department of Astronomy, 1 University Station C1400, Austin, Texas 78712-0259, USA

³ Astronomical Institute “Anton Pannekoek”, University of Amsterdam, PO Box 94249, 1090 GE Amsterdam, The Netherlands

⁴ Leiden Observatory, Leiden University, PO Box 9513, 2300 RA Leiden, The Netherlands

⁵ Dpt. de Física Teórica, Fac. de Ciencias, Universidad Autónoma de Madrid, Campus Cantoblanco, 28049 Madrid, Spain

⁶ Max Planck Institut für extraterrestrische Physik, Garching, Germany

⁷ Harvard-Smithsonian Center for Astrophysics, 60 Garden Street, MS 42, Cambridge, MA 02138, USA

⁸ Herschel Science Centre, European Space Astronomy Centre (ESA), P.O. Box 78, 28691 Villanueva de la Cañada (Madrid), Spain

⁹ Laboratoire d’Astrophysique de Grenoble, CNRS/Université Joseph Fourier (UMR5571) BP 53, F-38041 Grenoble cedex 9, France

¹⁰ Instituut voor Sterrenkunde, K.U.Leuven, Celestijnenlaan 200D, B-3001 Leuven, Belgium

¹¹ Department of Astronomy and Space Science, Astrophysical Research Center for the Structure and Evolution of the Cosmos, Sejong University, Seoul 143-747, Republic of Korea

¹² Caltech, Division of Geological & Planetary Sciences, Mail Code 150-21, Pasadena, CA 91125

¹³ Naval Research Laboratory, Code 7211, Washington, DC 20375, USA

¹⁴ National Optical Astronomy Observatory, 950 N. Cherry Ave., Tucson, AZ 85719, USA

¹⁵ Department of Astronomy, University of Maryland, College Park, MD 20742, USA

¹⁶ Institute for Astronomy, University of Hawaii at Manoa, Honolulu, HI 96822, USA

¹⁷ Department of Astronomy, The University of Michigan, 500 Church Street, Ann Arbor, MI 48109-1042, USA

¹⁸ Astronomy Department, University of California, Berkeley, CA 94720, USA

¹⁹ University of Vienna, Department of Astronomy, Türkenschanzstr. 17, 1180 Vienna, Austria

²⁰ SRON Netherlands Institute for Space Research, PO Box 800, 9700 AV, Groningen, The Netherlands

²¹ Department of Astrophysics/IMAPP, Radboud University Nijmegen, P.O. Box 9010 6500 GL Nijmegen The Netherlands

²² Centre for Star and Planet Formation, Natural History Museum of Denmark, University of Copenhagen, Øster Voldgade 5-7, DK-1350 Copenhagen K., Denmark